Supporting information

Fine-tuning the hierarchical morphology of multi-component organic photovoltaics via dual-additive strategy for 20.5% efficiency

Shitao Guan,[1] Yaokai Li,[1,2] ZhaoZhao Bi,[3] Yi Lin,[4] Yuang Fu,[5] Kangwei Wang,[6] Mengting Wang,[1] Wei Ma,[3] Jianlong Xia,[6] Zaifei Ma,[4] Zheng Tang,[4] Xinhui Lu,[5] Lijian Zuo,[1,2,] Hanying Li,[1] and Hongzheng Chen[1,2,*]*

S. Guan, Dr. Y. Li, C. Xu, M. Wang, Prof. L. Zuo, Prof. H. Li, and Prof. H. Chen
State Key Laboratory of Silicon and Advanced Semiconductor Materials, International Research Center for X Polymers, Department of Polymer Science and Engineering, Zhejiang University, Hangzhou 310027, P. R. China
E-mail: zjuzlj@zju.edu.cn; hzchen@zju.edu.cn

Dr. Y. Li, Prof. L. Zuo, and Prof. H. Chen
ZJU-Hangzhou Global Scientific and Technological Innovation Center, Hangzhou 310022, P. R. China

Dr. Z. Bi, and Prof. W. Ma
State Key Laboratory for Mechanical Behavior of Materials, Xi′an Jiaotong University, Xi'an 710049, P. R. China

Y. Lin, Prof. Z. Ma, Prof. Z. Tang
State Key Laboratory for Modification of Chemical Fibers and Polymer Materials, Center for Advanced Low-dimension Materials, College of Materials Science and Engineering, Donghua University, Shanghai 201620, P. R. China

Y. Fu, Prof. X. Lu
Department of Physics, The Chinese University of Hong Kong, New Territories, Hong Kong 999077, People's Republic of China

K. Wang, Prof. J. Xia
State Key Laboratory of Advanced Technology for Materials Synthesis andProcessing, Center of Smart Materials and Devices, Wuhan University of Technology,Wuhan 430070, P. R. China

Experimental Section

Materials

PM6 (Mn=45000 g/mol, Mw=97000 g/mol), D18-Cl (Mn=58507 g/mol, Mw=111618 g/mol), L8-BO, BTP-eC9 and PDINN were purchased from Solarmer Materials Inc. 2PACz was purchased from TCI Inc. All reagents and solvents were used directly as received.

OPV Fabrication

Organic solar cells were fabricated on ITO glass substrates with the conventional structure of ITO/2PACz/Active layer/ PDINN /Ag. The ITO glass substrates were cleaned by sonication using detergent, deionized water, acetone, and isopropanol consecutively for 20 min in each step before fabrication. The pre-cleaned Glass/ITO substrates were treated in an ultraviolet ozone generator for 20 min (LEBO Science UC100-SE), followed by deposition of 2PACz. The mixture of four components are weighted and dissolved together in CF and heated at 60 ℃ for 40 min before spin-coating. The active layer was spin coated at varied spinning speed for 30 s to form an active layer. Then the devices were annealed at 100 °C for 10 min. A layer of PDINN (0.5 mg/ml in methanol) was deposited by spin coating at 3500 rpm for 30 s. Then the Ag electrode with varied thickness was deposited by thermal evaporation under a base pressure of 5×10^{-4} Pa at the speed of 1 Å s^{-1}. The active cell areas with calibrated apertures are 0.06 cm^2 (0.0476 cm^2 covered by mask).

Device Characterization

Organic solar cells characterization under AM 1.5G spectra: The *J-V* measurement was performed via the solar simulator (SS-X50, Enlitech) along with AM 1.5G spectrum, whose intensity was calibrated by a standard silicon solar cell (SRC-2020, Enlitech) at 100 mW cm^{-2}. The external quantum efficiency (EQE) data was obtained from the solar-cell spectral-response measurement system (QE-R, Enlitech).

AFM characterization

Topographic images of the films, fabricated under the same optimized conditions, were measured from a VeecoMultiMode AFM in tapping mode, and the scanning rate for a 1 μm × 1 μm image was 1.0 Hz.

Contact Angle Measurement

Contact angles of water and diiodomethane on all films were measured using a contact angle system (DropMeter A-200, MAIST).

Grazing Incidence Small-Angle X-ray scattering (GISAXS) characterization

GISAXS measurements were performed using a Xeuss 2.0 SAXS/WAXS laboratory beamline using a Cu X-ray source (8.05 keV, 1.54 Å) and a Pilatus3R 300K detector. The incidence angle was 0.2°.

Grazing Incidence Wide-Angle X-ray Scattering (GIWAXS) characterization

GIWAXS measurements were performed at beamline 7.3.3 at the Advanced Light Source. Samples were prepared on Si substrates using identical blend solutions as those used in devices. The 10 keV X-ray beam was incident at a grazing angle of 0.10° -0.14°, selected to maximize the scattering intensity from the samples. The scattered x-rays were detected using a Dectris Pilatus 2M photon counting detector.

FT-IR Measurement

Fourier transform infrared spectroscopy (FT-IR) measurements were conducted on a Nicolet 6700 FTIR-ATR (Themo Fisher scientific LLC).

IR-AFM Measurement

IR-AFM images were obtained on nanoIR2-fs (Anasys Instruments) in the contact mode.

Transient Absorption Spectroscopy (TAS) Measurement

For femtosecond transient absorption spectroscopy, the fundamental output from Yb:KGW laser (1030 nm, 220 fs Gaussian fit, 100 kHz, Light Conversion Ltd) was separated to two light beams. One was introduced to NOPA (ORPHEUS-N, Light Conversion Ltd) to produce a certain wavelength for pump beam (here we use 750 nm,<10 μ J/cm2), the other was focused onto a YAG plate to generate white light continuum as probe beam. The pump and probe overlapped on the sample at a small angle less than 10°. The transmitted probe light from sample was collected by a linear CCD array.

We processed the analysis of hole transfer kinetics by biexponential fitting based on the following formula: $\boldsymbol{i} = \mathrm{A}_1\mathrm{e}^{-\mathrm{t}/\tau 1} + \mathrm{A}_2\mathrm{e}^{-\mathrm{t}/\tau 2}$

Electroluminescence External Quantum Efficiency (EQE_{EL})

A digital source meter (Keithley 2400) and a picoammeter (Keithley 6482) were used for the EQE_{EL} measurements. The former was applied to inject electric current into the solar cells to emit the photons, which will be collected using a Si diode and form electric current that can be measured by the latter.

Electroluminescence (EL) Measurement

A source meter (Keithley 2400) was employed to create the injected electric current leading to the luminescence of the solar cells. After going through an optical fiber(BFL200LS02, Thorlab), the emitted light emerged from the solar cells was collected by a fluorescence spectrometer (KYMERA-3281-B2, Andor Technology) including two sets of diffraction gratings for the wavelength range of 600~1100 nm and 900~1400 nm, and was measured by a Si EMCCD camera (DU970PBVF, Andor Technology) and an InGaAs camera (DU491A-1.7, Andor Technology), respectively.

The EL spectra were corrected for the optical losses in the fibers, the spectrometer and the cameras, using a calibrated halogen lamp (HL-3P-CAL, Ocean Optics Germany GmbH).

Photoluminescence (PL) Measurement

A Supercontinuous White Laser (SuperK EXU-6, NKT photonics) and narrowband filters (LLTF Contrast SR-VIS-HP8, LLTF Contrast SR-SWIR-HP8, NKT photonics) were used to acquire the tunable excitation wavelength. After excited by the laser, the measurement processes of the emission spectra were the same as electroluminescence spectra.

The PL spectra were corrected for the optical losses as same as EL spectra. In addition, the PL spectra were also corrected for excluding the difference of the absorption ability caused by thickness between different organic layers when characterize the photoluminescence quenching efficiency.

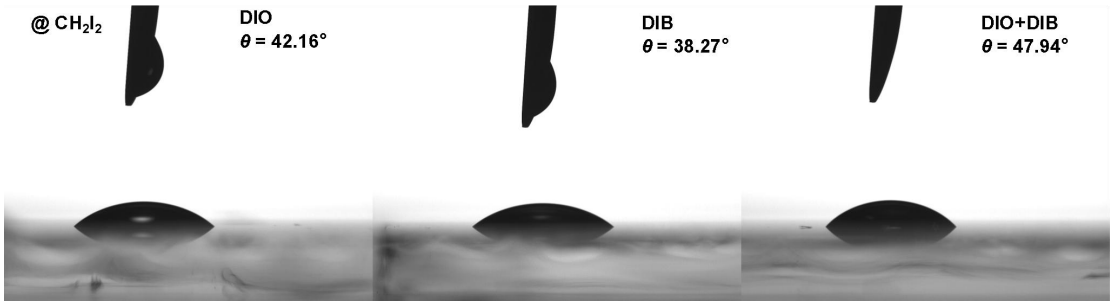

Figure S1. Contact angles of DIO, DIB, DIO+DIB with diiodomethane (CH_2I_2).

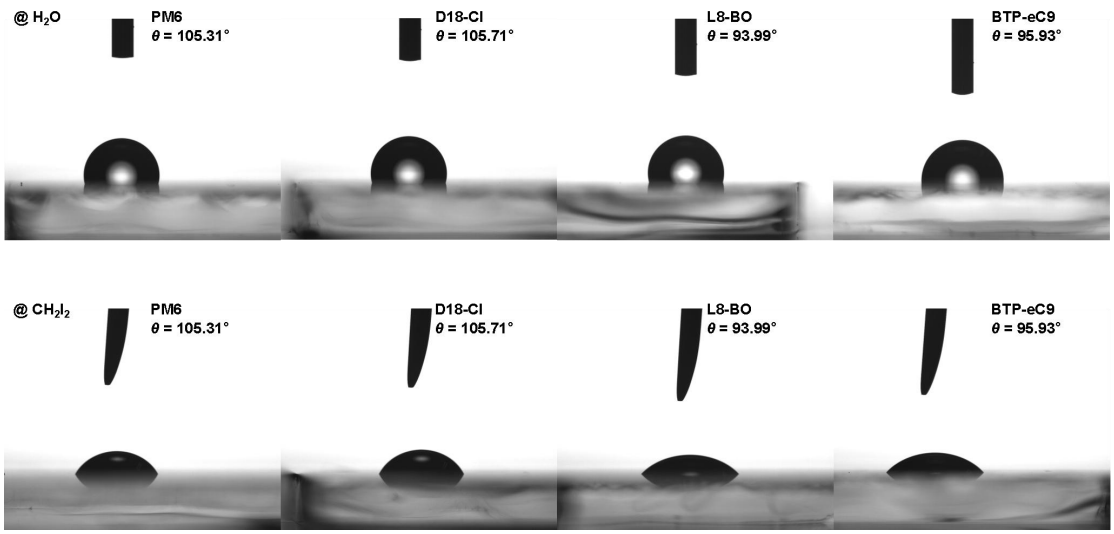

Figure S2. Contact angles of PM6, D18-Cl, L8-BO, BTP-eC9 with water (H_2O) and diiodomethane (CH_2I_2).

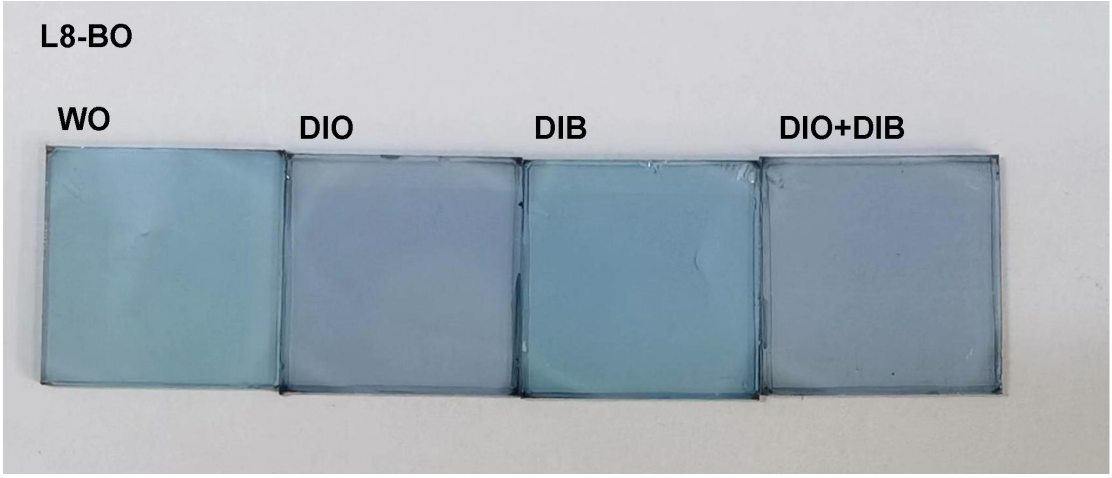

Figure S3. Images of L8-BO films with the corresponding additives.

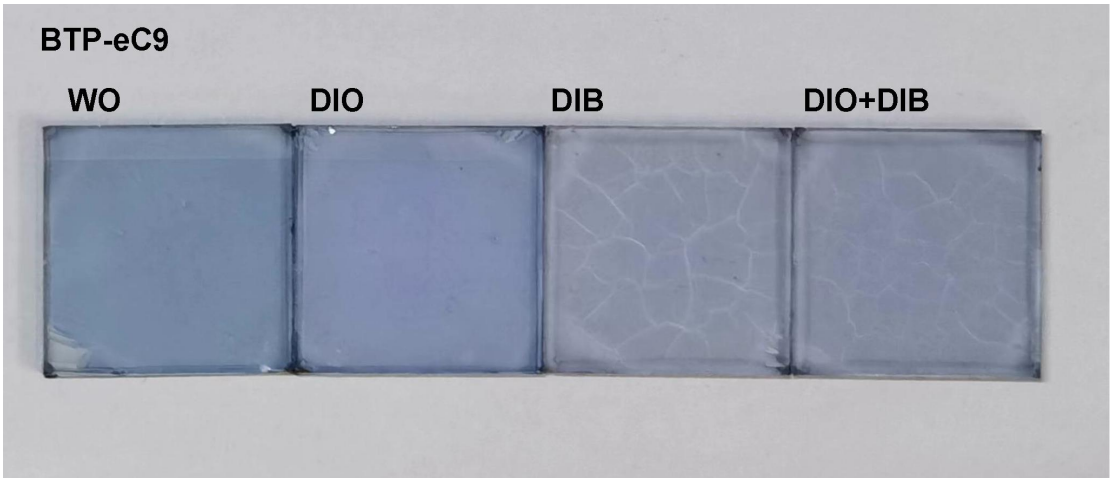

Figure S4. Images of BTP-eC9 films with the corresponding additives.

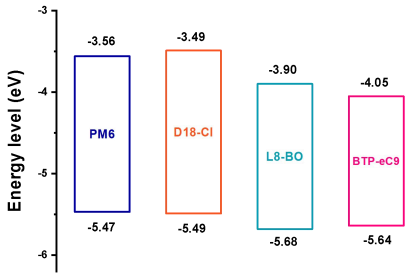

Figure S5. Energy levels of active layer materials PM6, D18-Cl, L8-BO, and BTP-eC9.

福建省计量科学研究院
FUJIAN METROLOGY INSTITUTE
（国家光伏产业计量测试中心）
National PV Industry Measurement and Testing Center

报告编号：23Q3-00160
Report No.

检测结果/说明：
Results of Test and Additional Explanation.

1 Standard Test Condition (STC)： Total Irradiance： 1000 W/m^2
Temperature： 25.0 ℃
Spectral Distribution： AM1.5G

2 Measurement Data and I-V/P-V Curves under STC

Forward Scan

I_{sc} (mA)	V_{oc} (V)	I_{MPP} (mA)	V_{MPP} (V)	P_{MPP} (mW)	FF (%)	η (%)
1.349	0.8769	1.248	0.7561	0.9436	79.77	19.82

Reverse Scan

I_{sc} (mA)	V_{oc} (V)	I_{MPP} (mA)	V_{MPP} (V)	P_{MPP} (mW)	FF (%)	η (%)
1.350	0.8805	1.254	0.7561	0.9481	79.76	19.92

Mismatch Factor: 0.9930

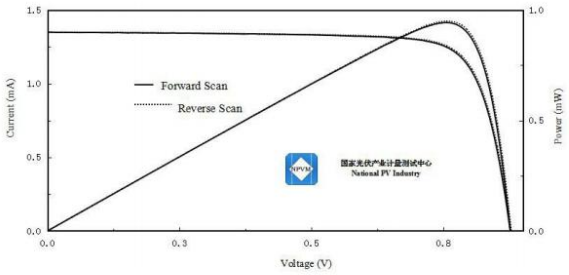

Figure 1. I-V and P-V characteristic curves of the measured sample under STC

Figure S6. The certification report of the champion OPV device.

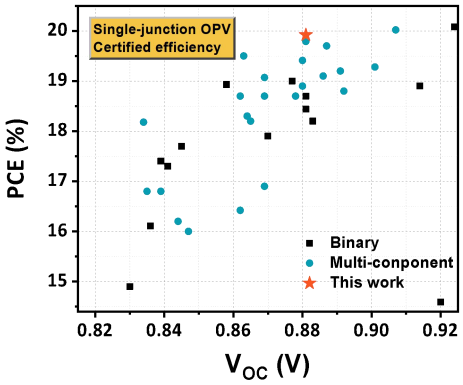

Figure S7. Figure-of-merit chart of certified single-junction OPVs.

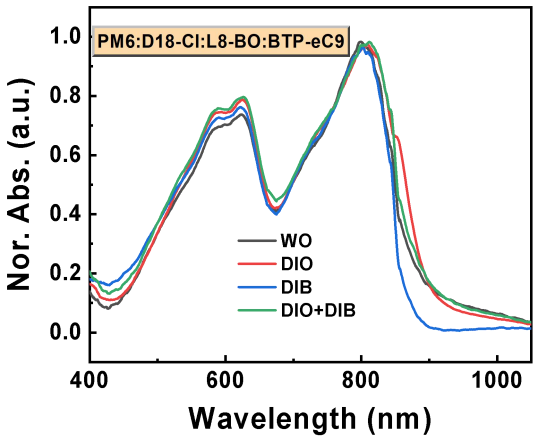

Figure S8. Normalized absorption spectra of PM6:D18-Cl:L8-BO:BTP-eC9 films with varied additives.

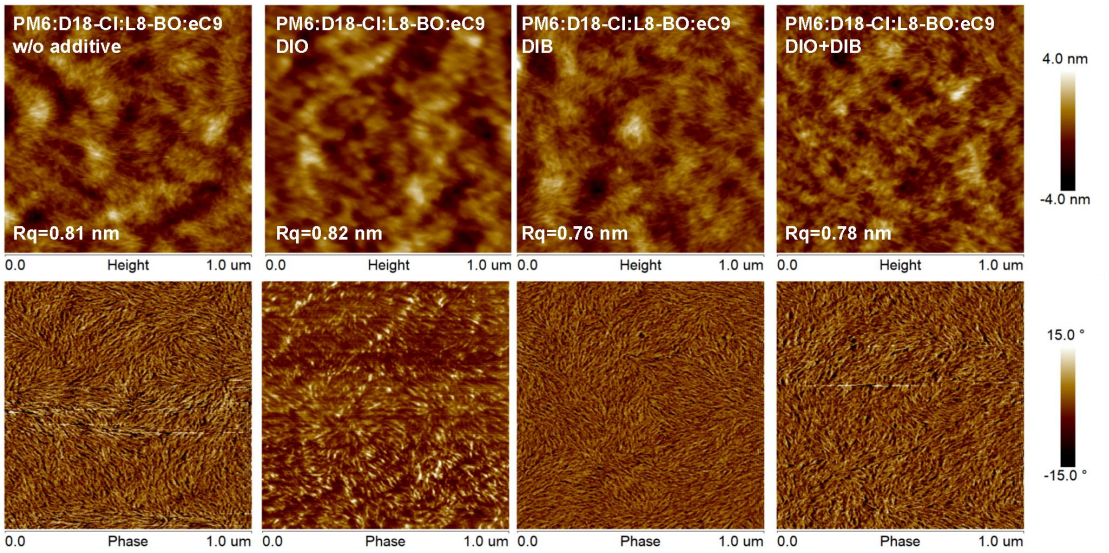

Figure S9. AFM height and phase images of PM6:D18-Cl:L8-BO:BTP-eC9 quaternary blend films based on the corresponding additives.

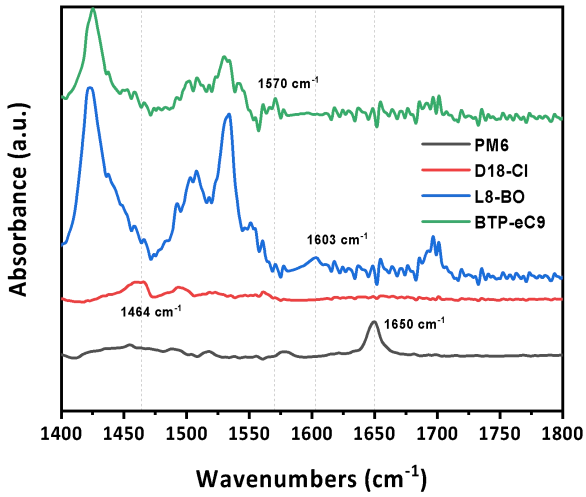

Figure S10. FTIR spectra of PM6, D18-Cl, L8-BO and BTP-eC9, where the characteristic wavenumbers are 1650, 1464, 1603, and 1570 cm^{-1}, respectively.

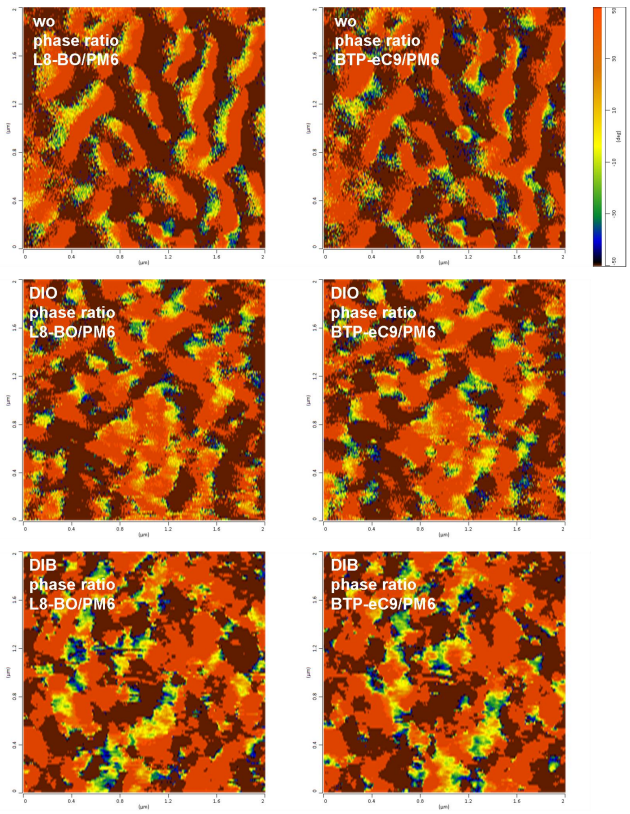

Figure S11. IR-AFM images of the calculated phase ratio of L8-BO and BTP-eC9 in comparison to PM6 based on films without additive, and films with DIO, DIB.

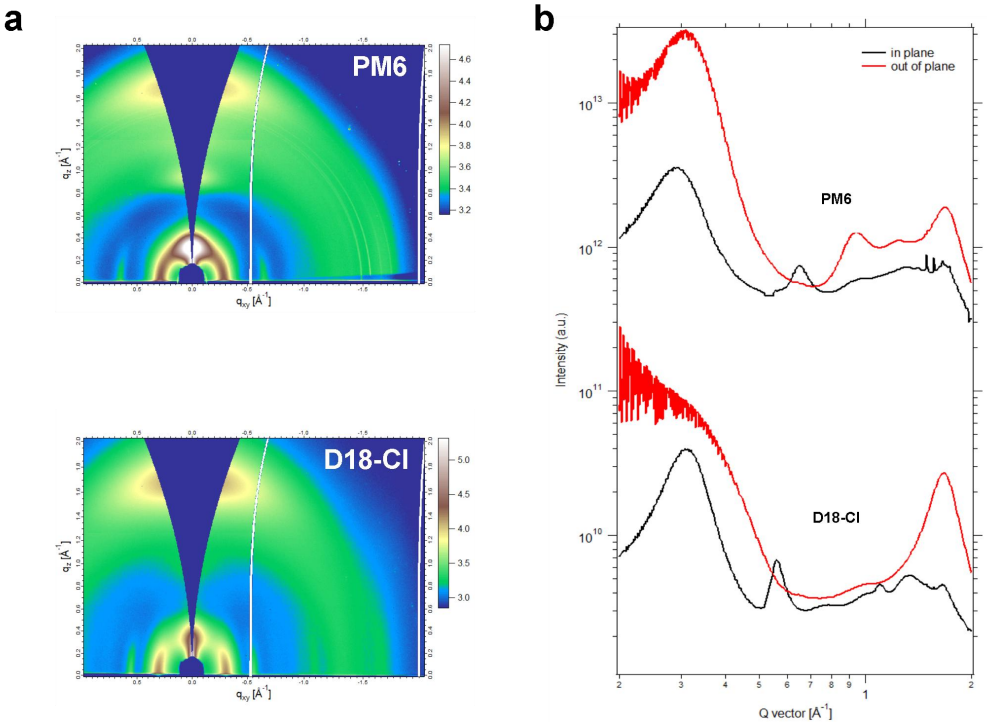

Figure S12. The 2D GIWAXS patterns of donors PM6 and D18-Cl. q_{xy}, scattering vector in the in-plane (IP) direction; q_z, scattering vector in the out-of-plane (OOP) direction. (b) IP and OOP line cut profiles of the 2D GIWAXS data.

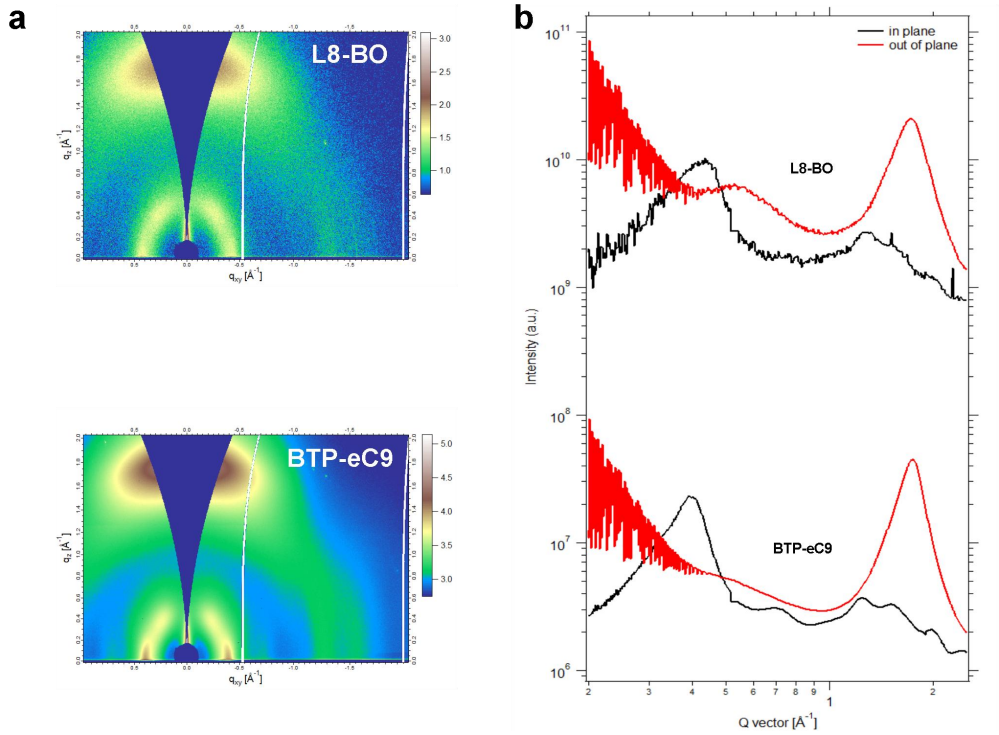

Figure S13. The 2D GIWAXS patterns of acceptors L8-BO and BTP-eC9. (b) IP and OOP line cut profiles of the 2D GIWAXS data.

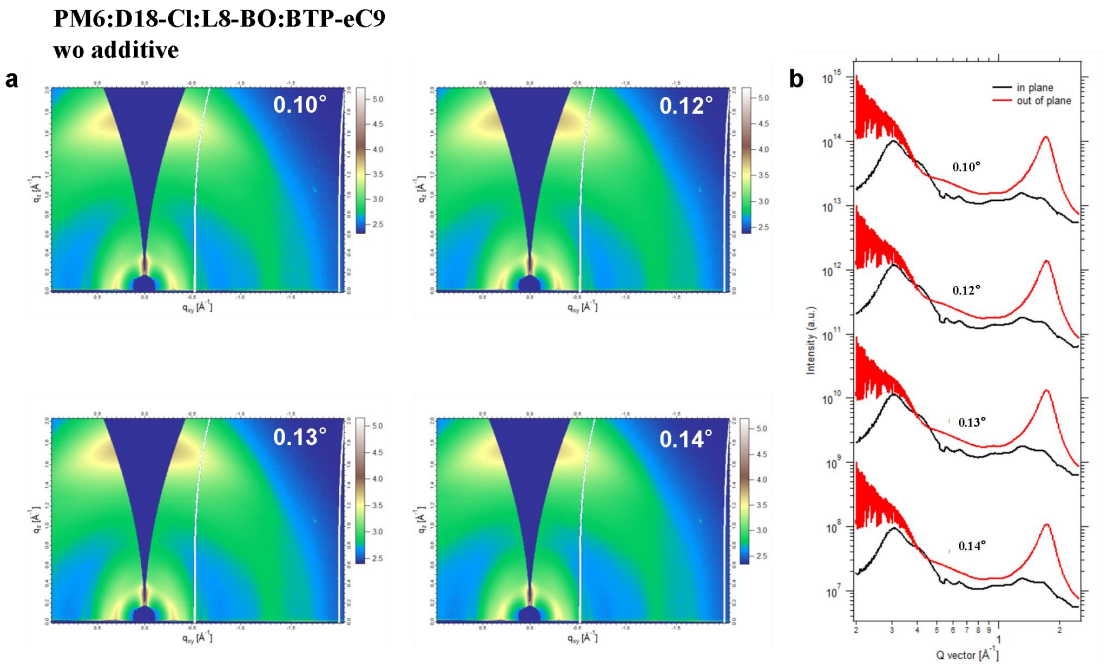

Figure S14. The 2D GIWAXS patterns of PM6:D18-Cl:L8-BO:BTP-eC9 quaternary blend without additive. (b) IP and OOP line cut profiles of the 2D GIWAXS data.

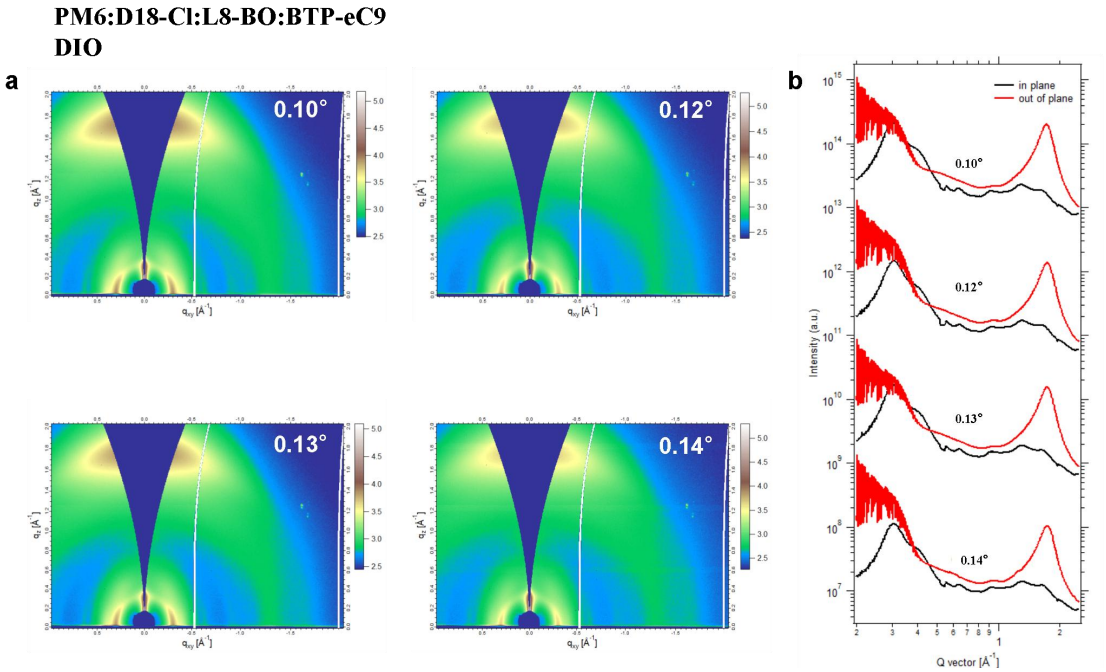

Figure S15. The 2D GIWAXS patterns of PM6:D18-Cl:L8-BO:BTP-eC9 quaternary blend with DIO additive. (b) IP and OOP line cut profiles of the 2D GIWAXS data.

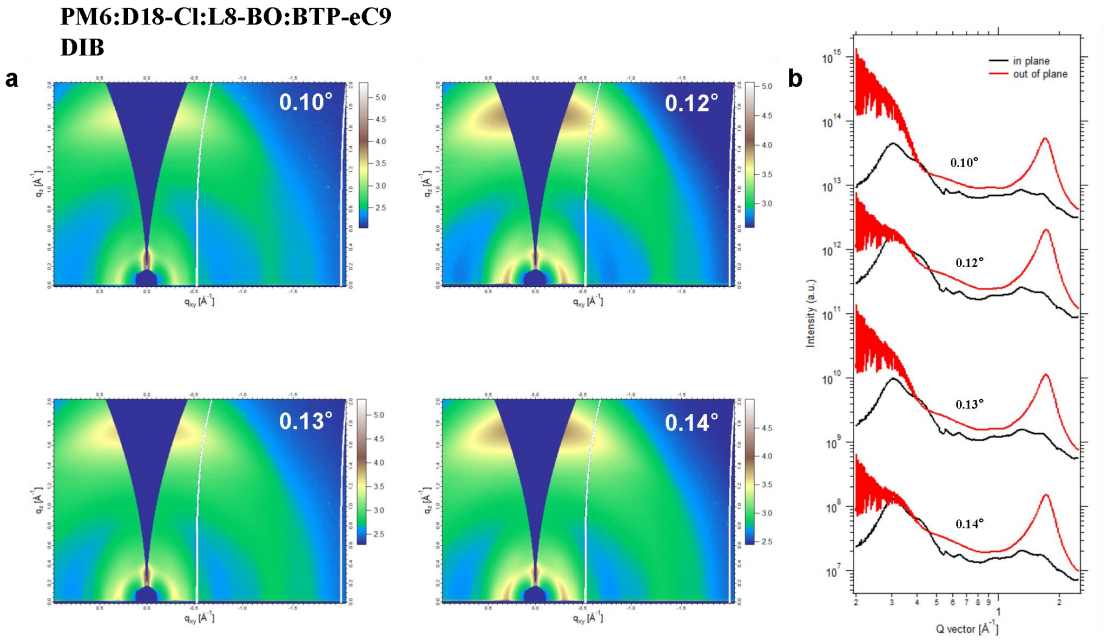

Figure S16. The 2D GIWAXS patterns of PM6:D18-Cl:L8-BO:BTP-eC9 quaternary blend with DIB additive. (b) IP and OOP line cut profiles of the 2D GIWAXS data.

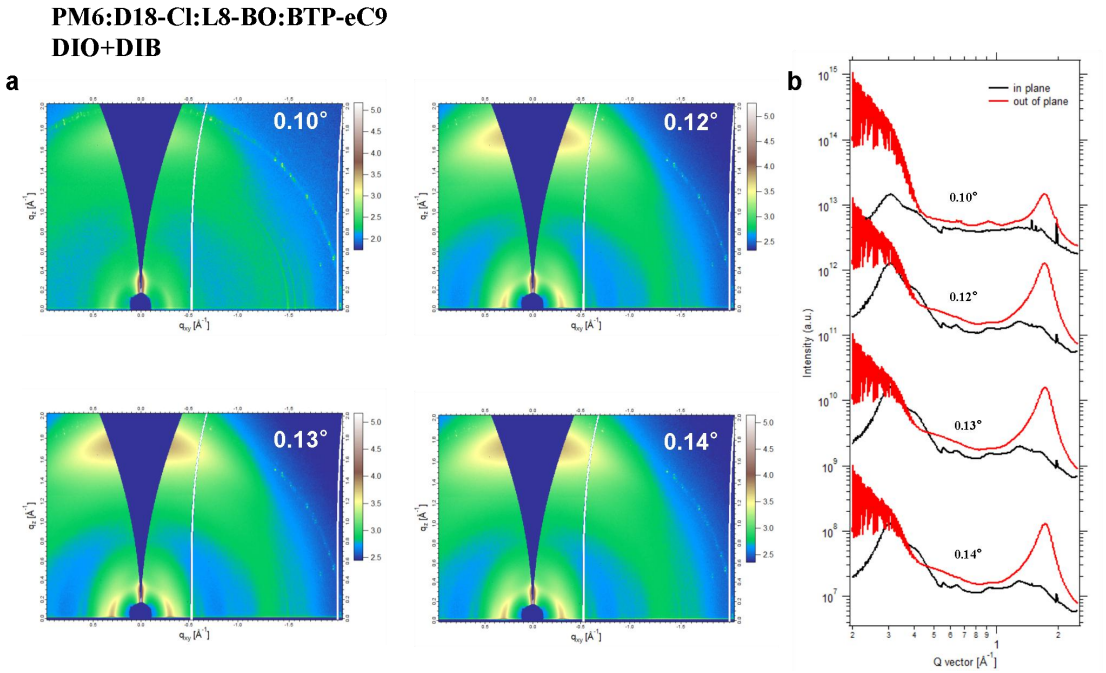

Figure S17. The 2D GIWAXS patterns of PM6:D18-Cl:L8-BO:BTP-eC9 quaternary blend with DIO+DIB additive. (b) IP and OOP line cut profiles of the 2D GIWAXS data.

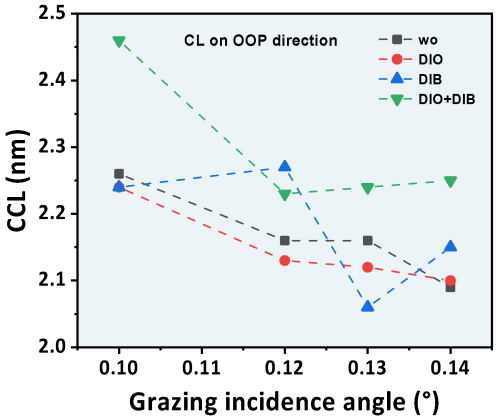

Figure S18. CCL values calculated from the GIWAXS measurement with beam incidents at a grazing angle of 0.10°-0.14° of the additive-free, DIO, DIB, DIO+DIB based quaternary blends

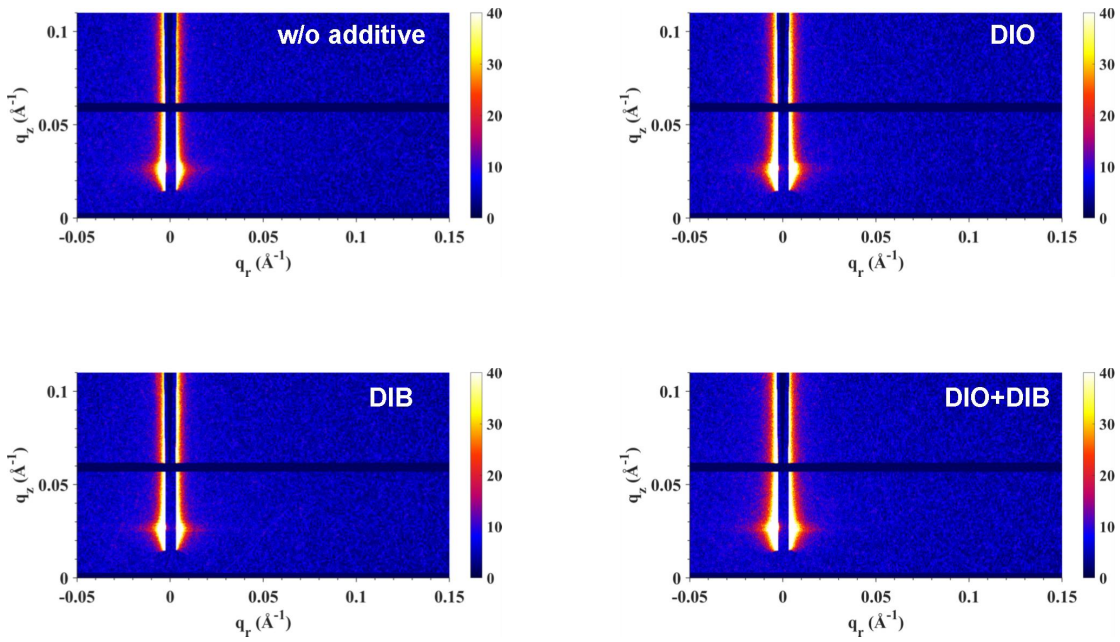

Figure S19. GISAXS patterns of quaternary blend based on the corresponding additives.

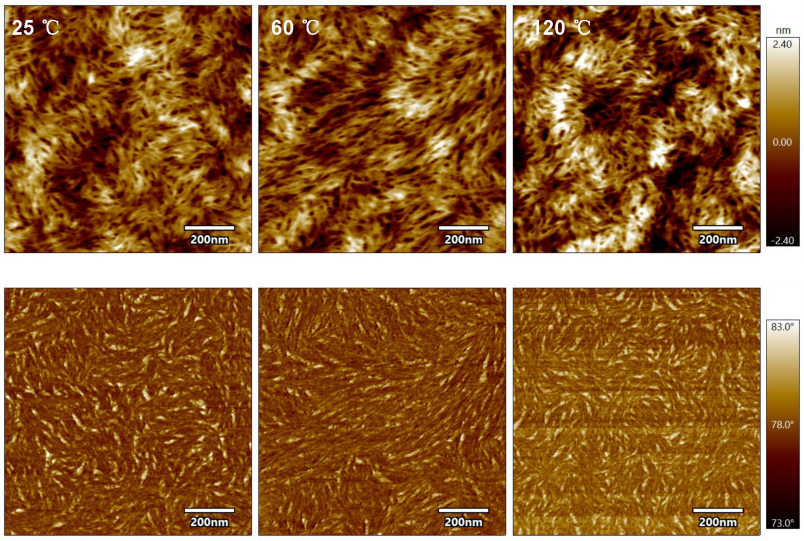

Figure S20. AFM height and phase images of the quaternary blend films with the DIO+DIB additive processed at 25, 60, and 120 ℃.

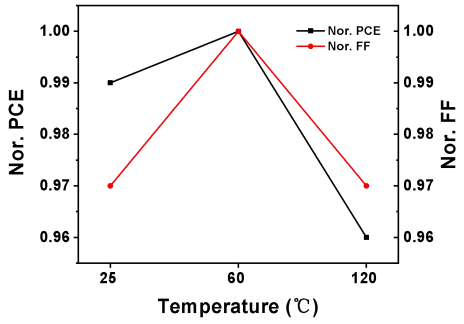

Figure S21. Normalized PCE and FF of the dual-additive based devices dissolved and cast at 25, 60, and 120 ℃.

Note:

Moreover, molecular interaction and pre-aggregation are sensitive to the dissolving temperature while spinodal decomposition and phase separation are highly sensitive to the solution temperature. To examine how temperature influences the morphology, an experiment is designed by comparing quaternary blends dissolved and cast at different temperatures: 25 ℃ (room temperature), 60 ℃ and 120 ℃. Although all these three blends are all dissolved macroscopically, however, the intermixing may vary on a molecular level (**Figure S20**). The OPV devices with normalized PCE and FF presented in **Figure S21** for intuitive observation. Blends with too low (25 ℃) or too high temperature (120 ℃) show inferior performance than the film cast at the optimal condition(60 ℃), especially affecting FF of the devices, which may be due to that low temperature cannot form appropriate molecular interaction while high temperature cause inferior film formation kinetics.

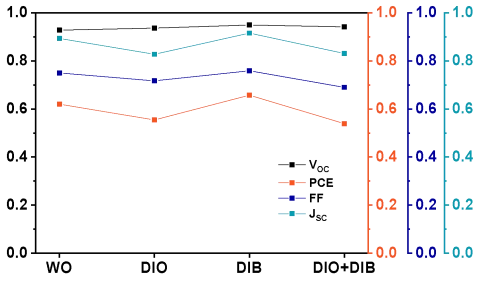

Figure S22. Normalized PCE, V_{OC}, J_{SC} and FF of the OPV devices with different additives. The initial values are set to 1.

Note:

Further, an accelerated aging test is conducted with the completed devices with different additives heated at 90 ℃ for 100 hours in the N2-filled glovebox to study the morphology stability (**Figure S22**). As a result, the DIB based devices and the devices without additive show better morphology stability than the devices containing DIO, which is difficult to evaporate and remains in the bulk (**Figure S1**), further deteriorating the already-optimized morphology. Therefore, the main reasons for the impact of DIO on long-term stability on morphology should be explored while alternative additives should also be screened in the future.

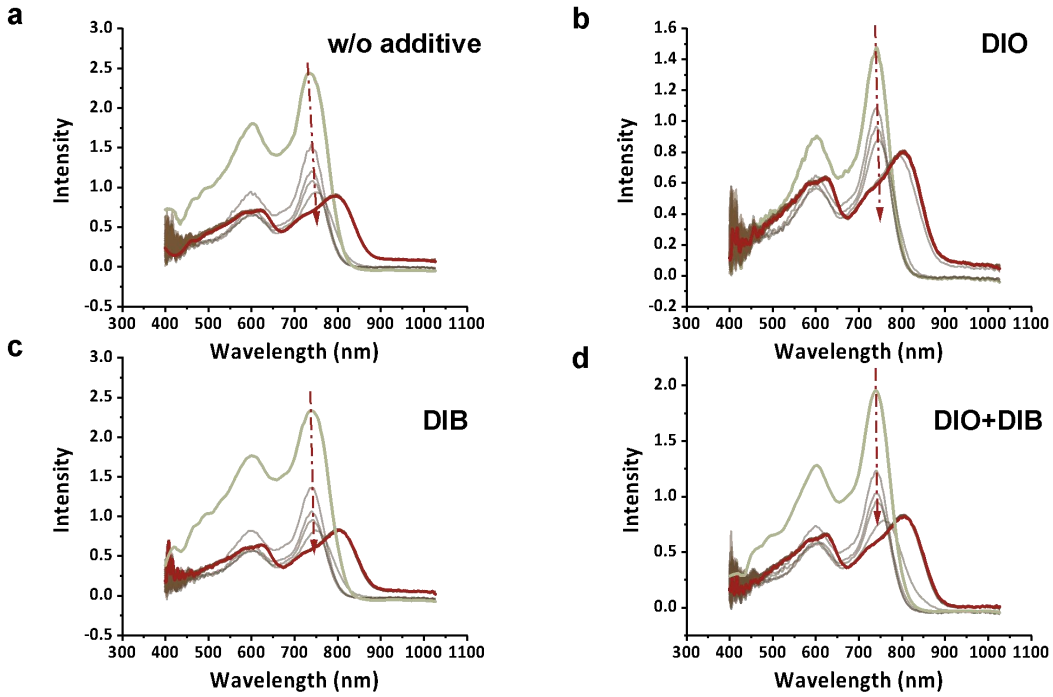

Figure S23. Detailed film formation process of the PM6:D18-Cl:L8-BO:BTP-eC9 quaternary blend based on various additives (a) without additive, (b) DIO, (c) DIB, (d) DIO+DIB.

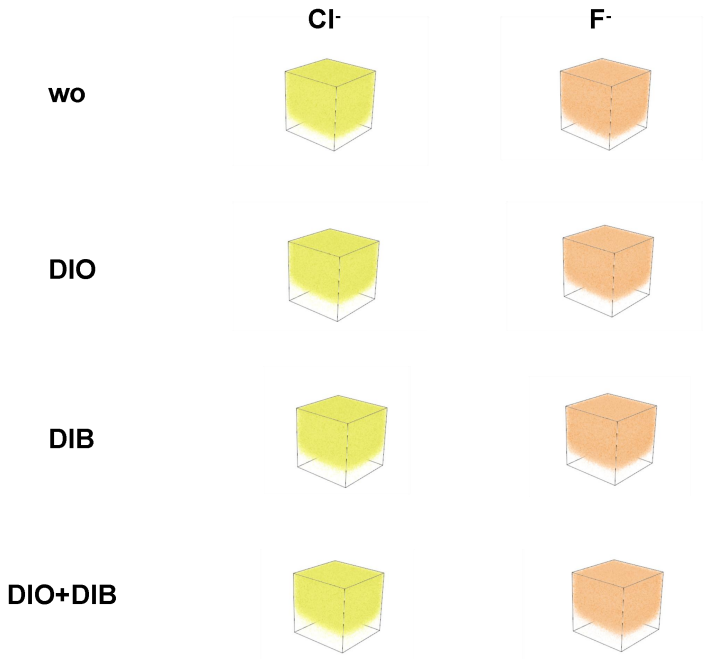

Figure S24. 3D diagrams of Cl^- and F^- distribution in quaternary blend films based on additive-free, DIO, DIB, and DIO+DIB.

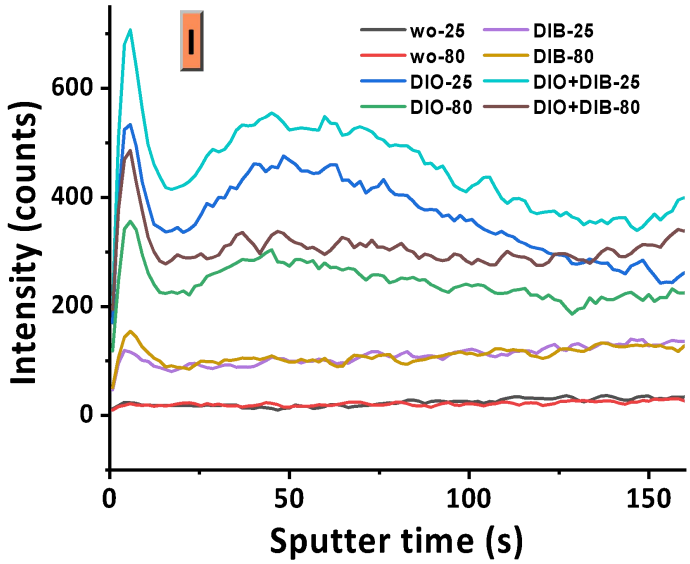

Figure S25. I^- distribution in quaternary blend films, where 25 represents the film without annealing while 80 represents the film annealed at 80℃ for 5 min.

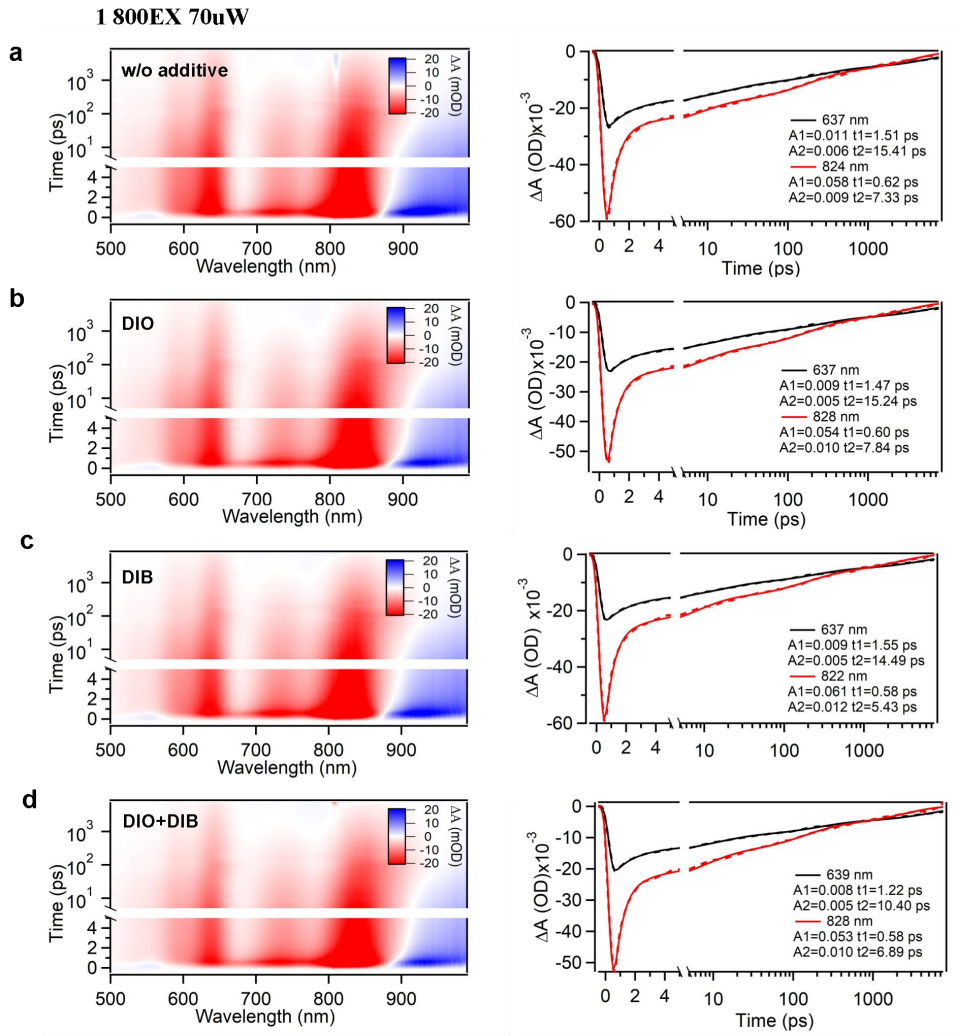

Figure S26. (a) The color plot of transient absorption spectra of PM6:D18-Cl:L8-BO:BTP-eC9 blend films under 800 nm excitation. (b) The corresponding 2D plots of TAS measurement.

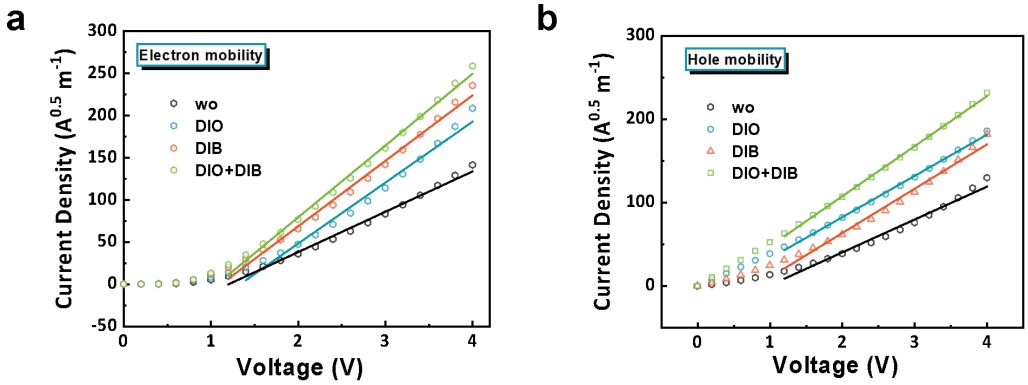

Figure S27. Electron and hole mobility of the quaternary electron-only and hole-only devices.

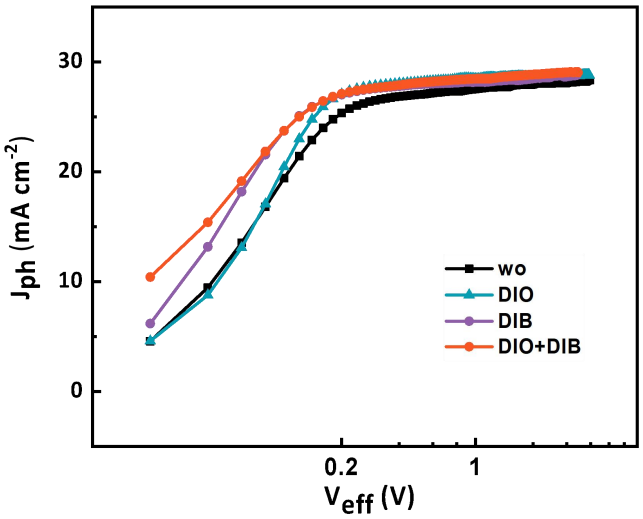

Figure S28. J_{ph} versus V_{eff} of the corresponding devices.

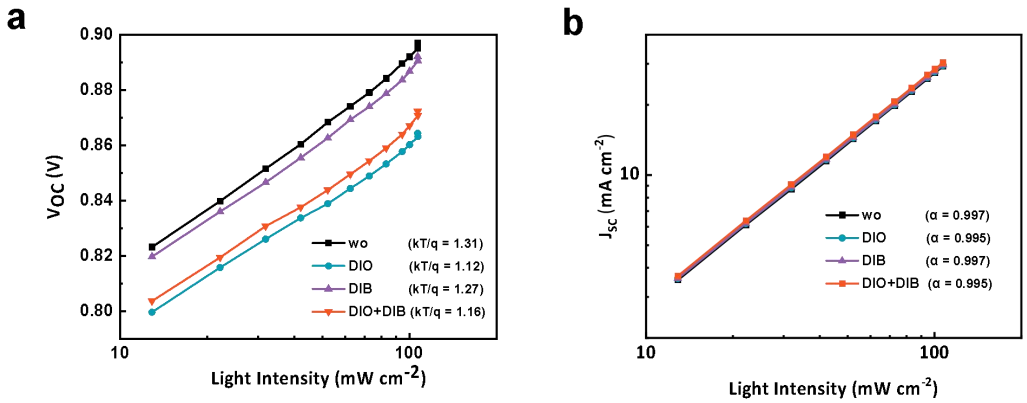

Figure S29. Dependence of 1)V_{OC} and 2) J_{SC} on various light intensities based on the quaternary OPVs without additive, and DIO, DIB, DIO+DIB based devices.

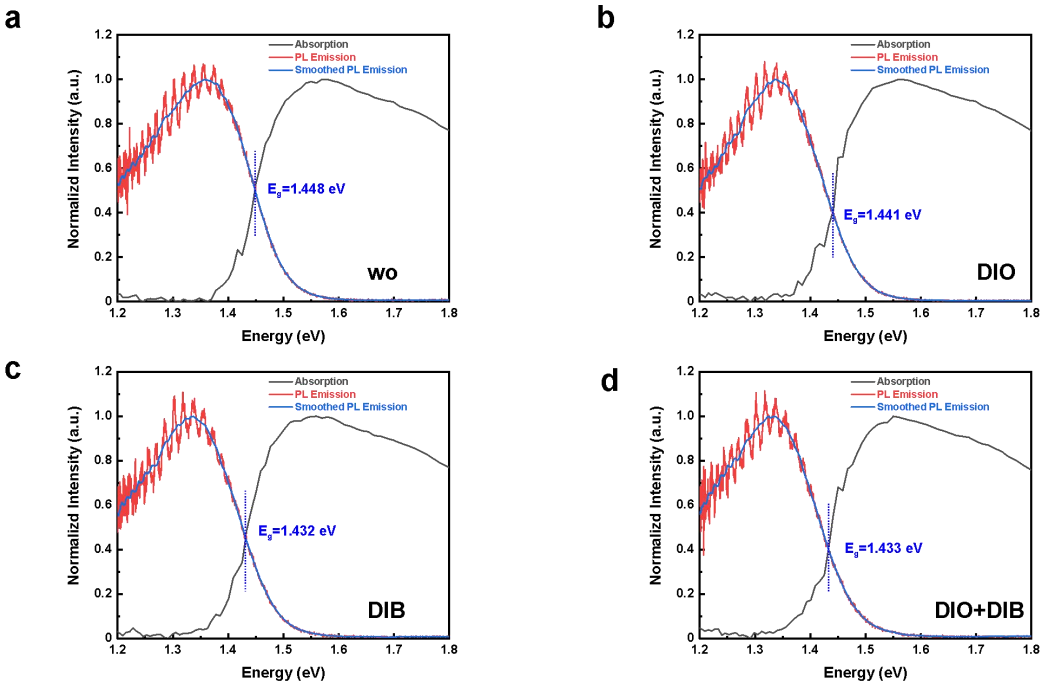

Figure S30. Eg plots determined from the intersection of the absorption and the PL emission.

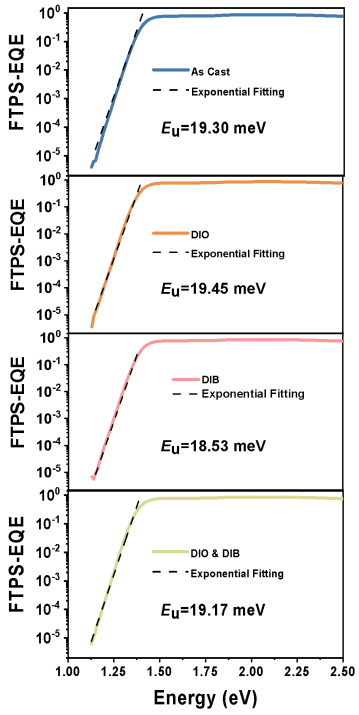

Figure S31. The calculation of Urbach energy (E_U) for PM6:D18-Cl:L8-BO:BTP-eC9 based OPVs with the corresponding additives.

Table S1. Contact angles of the photo-active materials PM6, D18-Cl, L8-BO, BTP-eC9 and the additives DIO, DIB, DIO+DIB.

Film	θ_{H2O} (°)	θ_{CH2I2}(°)	Surface tension(mJ cm^{-2})
PM6	105.31	61.77	27.13
D18-Cl	105.71	63.46	26.58
L8-BO	93.99	44.89	45.18
BTP-eC9	95.93	38.87	41.72
DIO	40.64	42.16	173.58
DIB	32.24	38.27	191.91
DIO+DIB	39.65	47.94	175.88

Table S2. calculated Flory–Huggins parameter (χ) of the corresponding additives with the photo-active materials.

Film	Surface tension(mJ cm^{-2})	$\chi_{D/A,DIO}$	$\chi_{D/A,DIB}$	$\chi_{D/A,DIO+DIB}$
PM6	27.13	63.46	74.73	64.85
D18-Cl	26.58	64.31	75.65	65.71
L8-BO	45.18	41.65	50.86	42.78
BTP-eC9	41.72	45.10	54.67	46.28

Note:

The Flory-Huggins parameter (χ) between photo-active material (donor or acceptor, D/A) and additives is calculated as:

$$\chi_{D/A,\,Add} = (\sqrt{D/A} - \sqrt{Add})^2$$

Table S3. Certified efficiencies of the state-of-art OPVs.

Device	V_{OC} (V)	J_{SC} (mA cm^{-2})	FF (%)	PCE (%)	Ref.
PM6:D18-Cl:L8-BO:BTP-eC9	0.881	28.34	79.76	19.92	**This work**
PTO2:IT-4F	0.92	21.75	72	14.59	[1]
PM6:Y6	0.83	23.2	76.8	14.9	[2]
PM6:Y6:PC71BM	0.847	24.71	76.6	16	[3]
PM6:Y11	0.836	26.3	73.32	16.11	[4]
PM6:Y6:PC61BM	0.844	25.63	74.7	16.2	[5]
PM6:N3:PC71BM	0.862	26.2	72.7	16.42	[6]
PM6:Y6:MF1	0.839	25.51	78.4	16.8	[7]
PM6:DRTB-T-C4:Y6	0.835	25.69	78.3	16.8	[8]
PM6:BTTzR:Y6	0.869	25.11	77.5	16.9	[9]
PBDB-TF::BTP-eC9	0.841	26.2	78.3	17.3	[10]
PM6:BTP-S9	0.839	26.84	77.1	17.4	[11]
PM6:Y6	0.845	26.43	79.1	17.7	[12]
PM6:L8-BO	0.87	25.38	81	17.9	[13]
D18/T9TBO-F:Y6-O	0.834	29.0	75.11	18.18	[14]
PM6:BO-4Cl:BO-5Cl	0.865	26.88	78.2	18.2	[15]
PM6:L8-BO	0.883	26.09	79	18.2	[16]
PBDB-TF:HDO-4Cl:eC9	0.864	26.68	79.5	18.3	[17]
PBDB-TF:BTP-eC9:BTP-S2	0.878	26.55	78.57	18.31	[18]
PM6/L8-BO	0.881	26.52	79	18.44	[19]
PM1:L8-BO:BTP-2F2Cl	0.869	27.19	79	18.7	[20]
PBQx-TF:eC9-2Cl:F-BTA3	0.878	26.8	79.4	18.7	[21]
PM6:BTP-eC9:BTP-S9	0.862	27.37	79	18.7	[22]
PM6:L8-BO-T2	0.881	27.07	78.3	18.7	[23]
PM6:BTP-H2:L8BO	0.892	26.42	79.7	18.8	[24]
D18/L8-BO	0.914	26.54	77.8	18.9	[25]
PBDB-TCl:AITC:BTP-eC9	0.88	26.9	79.6	18.9	[26]
PBQx-TF:eC9-2Cl	0.877	27.1	79.8	19.0	[27]
PM6:L8-BO:BTP-eC9	0.869	27.47	79.86	19.07	[28]
PBQx-TCl:PBDB-TF:eC9-2Cl	0.886	26.99	79.7	19.1	[29]
D18-Cl:BTP-eC9/PM6:L8-BO	0.901	26.86	79.67	19.28	[30]
PM6:D18:L8-BO	0.891	26.7	80.8	19.2	[31]
PM6:BTP-eC9:BTP S16:BTP-S17	0.88	27.73	79.55	19.41	[32]
PM6:D18-2F:BTP-eC9	0.863	28.67	78.79	19.50	[33]
PB2:BTP-eC9:FTCC-Br	0.887	27.54	80.72	19.7	[34]
PM6:L8-BO:BTP-eC9	0.881	27.85	80.66	19.79	[35]
D18:Z8:L8-BO	0.902	27.0	81.04	19.8	[36]
D18:L8-ThCl/L8-BO:L8-ThCl	0.907	27.4	80.44	20.02	[37]
D18-Cl:BTP-4F-P2EH	0.924	27.47	79.11	20.08	[38]

Table S4. The photovoltaic performance comparison of PM6:D18:L8-BO:BTP-eC9 and PM6:D18-Cl:L8-BO:BTP-eC9.

	V_{OC} (V)	J_{SC} (mA cm^{-2})	FF (%)	PCE (%)
PM6:D18:L8-BO:BTP-eC9	0.872	28.25	81.80	20.14
	(0.869 ± 0.003)	(28.01 ± 0.31)	(81.08 ± 0.53)	(19.71 ± 0.30)
PM6:D18-Cl:L8-BO:BTP-eC9	0.879	28.55	81.33	20.52
	(0.874 ± 0.01)	(28.54 ± 0.18)	(80.91 ± 0.44)	(20.31 ± 0.12)

Table S5. Structure parameters including position, FWHM, d-spacing, CCL of PM6 film.

In plane							
Location($Å^{-1}$)	d-spacing(Å)	FWHM	CL(nm)	Location($Å^{-1}$)	d-spacing(Å)	FWHM	CL(nm)
0.289	21.74	0.085	6.65	1.67	3.77	0.27	2.09
0.652	9.64	0.066	8.57	-	-	-	-
Out of plane							
Location($Å^{-1}$)	d-spacing(Å)	FWHM	CL(nm)	Location($Å^{-1}$)	d-spacing(Å)	FWHM	CL(nm)
0.305	20.60	0.079	7.16	0.305	-	-	-
0.958	6.56	0.222	2.55	0.958	-	-	-
1.664	3.78	0.371	1.52	1.664	-	-	-
0.305	20.60	0.079	7.16	0.305	-	-	-
0.958	6.56	0.222	2.55	0.958	-	-	-

Table S6. Structure parameters including position, FWHM, d-spacing, CCL of D18-Cl film.

In plane							
Location($Å^{-1}$)	d-spacing(Å)	FWHM	CL(nm)	Location($Å^{-1}$)	d-spacing(Å)	FWHM	CL(nm)
0.309	20.33	0.074	7.64	1.63	3.85	0.27	2.13
1.348	4.66	0.339	1.67	-	-	-	-
Out of plane							
Location($Å^{-1}$)	d-spacing(Å)	FWHM	CL(nm)	Location($Å^{-1}$)	d-spacing(Å)	FWHM	CL(nm)
1.663	3.78	0.258	2.19	1.663	-	-	-

Table S7. Structure parameters including position, FWHM, d-spacing, CCL of L8-BO film.

In plane							
Location(Å^{-1})	d-spacing(Å)	FWHM	CL(nm)	Location(Å^{-1})	d-spacing(Å)	FWHM	CL(nm)
0.42	14.96	0.114	4.96	0.42	14.96	0.114	4.96
1.289	4.87	0.263	2.15	1.289	4.87	0.263	2.15
Out of plane							
Location(Å^{-1})	d-spacing(Å)	FWHM	CL(nm)	Location(Å^{-1})	d-spacing(Å)	FWHM	CL(nm)
0.51	12.32	0.307	1.84	0.51	-	-	-
1.711	3.67	0.33	1.71	1.711	-	-	-

Table S8. Structure parameters including position, FWHM, d-spacing, CCL of BTP-eC9 film.

In plane							
Location(Å^{-1})	d-spacing(Å)	FWHM	CL(nm)	Location(Å^{-1})	d-spacing(Å)	FWHM	CL(nm)
0.391	16.07	0.09	6.28	1.25	5.01	0.27	2.12
0.67	9.38	0.296	1.91	1.49	-	0.39	-
Out of plane							
Location(Å^{-1})	d-spacing(Å)	FWHM	CL(nm)	Location(Å^{-1})	d-spacing(Å)	FWHM	CL(nm)
1.73	3.63	0.253	2.24	1.73	3.63	0.253	-

Table S9. Structure parameters including position, FWHM, d-spacing, CCL of the quaternary blended film without additive.

0.1°	In plane			
	Location(Å^{-1})	d-spacing(Å)	FWHM	CL(nm)
	0.309	20.33	0.082	6.90
	1.313	4.79	0.245	2.31
	1.58	3.98	0.67	0.84
	Out of plane			
	Location(Å^{-1})	d-spacing(Å)	FWHM	CL(nm)
	1.709	3.68	0.25	2.26
0.12°	In plane			
	Location(Å^{-1})	d-spacing(Å)	FWHM	CL(nm)
	0.311	20.20	0.086	6.58
	1.33	4.72	0.324	1.75
	1.59	3.94	0.6	0.94
	Out of plane			
	1.721	3.65	0.262	2.16
0.13°	In plane			
	Location(Å^{-1})	d-spacing(Å)	FWHM	CL(nm)
	0.311	20.20	0.087	6.50
	1.323	4.75	0.329	1.72
	1.59	3.94	0.56	1.00
	Out of plane			
	1.721	3.65	0.262	2.16
0.14°	In plane			
	Location(Å^{-1})	d-spacing(Å)	FWHM	CL(nm)
	0.311	20.20	0.087	6.50
	1.333	4.71	0.307	1.84
	1.6	3.94	0.58	0.98
	Out of plane			
	1.723	3.65	0.27	2.09

Table S10. Structure parameters including position, FWHM, d-spacing, CCL of the quaternary blended film with DIO additive.

0.1°	In plane			
	Location($Å^{-1}$)	d-spacing(Å)	FWHM	CL(nm)
	0.305	20.60	0.065	8.70
	1.304	4.82	0.245	2.31
	1.58	3.98	0.6	0.94
	Out of plane			
	Location($Å^{-1}$)	d-spacing(Å)	FWHM	CL(nm)
	1.715	3.66	0.252	2.24
0.12°	In plane			
	Location($Å^{-1}$)	d-spacing(Å)	FWHM	CL(nm)
	0.308	20.40	0.069	8.20
	1.318	4.77	0.26	2.17
	1.6	3.94	0.59	0.96
	Out of plane			
	1.729	3.63	0.265	2.13
0.13°	In plane			
	Location($Å^{-1}$)	d-spacing(Å)	FWHM	CL(nm)
	0.307	20.47	0.062	9.12
	1.317	4.77	0.268	2.11
	1.59	3.95	0.59	0.96
	Out of plane			
	1.729	3.63	0.267	2.12
0.14°	In plane			
	Location($Å^{-1}$)	d-spacing(Å)	FWHM	CL(nm)
	0.308	20.40	0.059	9.58
	1.322	4.75	0.27	2.09
	1.6	3.94	0.53	1.07
	Out of plane			
	1.731	3.63	0.269	2.10

Table S11. Structure parameters including position, FWHM, d-spacing, CCL of the quaternary blended film with DIB additive.

0.1°	In plane			
	Location(Å^{-1})	d-spacing(Å)	FWHM	CL(nm)
	0.308	20.40	0.088	6.43
	1.309	4.80	0.243	2.33
	1.61	3.91	0.54	1.05
	Out of plane			
	Location(Å^{-1})	d-spacing(Å)	FWHM	CL(nm)
	1.705	3.69	0.252	2.24
0.12°	In plane			
	Location(Å^{-1})	d-spacing(Å)	FWHM	CL(nm)
	0.312	20.14	0.087	6.50
	1.326	4.74	0.261	2.17
	1.59	3.96	0.56	1.02
	Out of plane			
	1.722	3.65	0.249	2.27
0.13°	In plane			
	Location(Å^{-1})	d-spacing(Å)	FWHM	CL(nm)
	0.31	20.27	0.088	6.43
	1.324	4.75	0.279	2.03
	1.57	4.01	0.75	0.75
	Out of plane			
	1.716	3.66	0.274	2.06
0.14°	In plane			
	Location(Å^{-1})	d-spacing(Å)	FWHM	CL(nm)
	0.312	20.14	0.088	6.43
	1.329	4.73	0.251	2.25
	1.57	4.00	0.72	0.79
	Out of plane			
	1.722	3.65	0.263	2.15

Table S12. Structure parameters including position, FWHM, d-spacing, CCL of the quaternary blended film with DIO+DIB additive.

0.1°	In plane			
	Location($Å^{-1}$)	d-spacing(Å)	FWHM	CL(nm)
	0.308	20.40	0.071	7.96
	Out of plane			
	Location($Å^{-1}$)	d-spacing(Å)	FWHM	CL(nm)
	1.71	3.67	0.23	2.46
0.12°	In plane			
	Location($Å^{-1}$)	d-spacing(Å)	FWHM	CL(nm)
	0.307	20.47	0.069	8.20
	1.311	4.79	0.277	2.04
	1.59	3.95	0.47	1.20
	Out of plane			
	1.714	3.67	0.254	2.23
0.13°	In plane			
	Location($Å^{-1}$)	d-spacing(Å)	FWHM	CL(nm)
	0.308	20.40	0.054	10.47
	1.314	4.78	0.249	2.27
	1.58	3.98	0.59	0.95
	Out of plane			
	1.723	3.65	0.252	2.24
0.14°	In plane			
	Location($Å^{-1}$)	d-spacing(Å)	FWHM	CL(nm)
	0.31	20.27	0.069	8.20
	1.316	4.77	0.269	2.10
	1.57	3.99	0.54	1.04
	Out of plane			
	1.723	3.65	0.251	2.25

Table S13. μ_e and μ_h of the queternary devices calculated from the SCLC measurements based on variant additives.

Device	μ_e($\times10^{-4}$ cm^2 V^{-1} s^{-1})	μ_h($\times10^{-4}$ cm^2 V^{-1} s^{-1})
wo	5.98 ± 0.69	4.50 ± 1.36
DIO	8.96 ± 1.41	8.50 ± 0.86
DIB	10.11 ±2.93	9.19 ± 1.74
DIO+DIB	12.32 ± 2.97	10.50 ± 1.81

Table S14. η_{diss} and η_{coll} of the queternary devices based on variant additives.

	wo	**DIO**	**DIB**	**DIO+DIB**
η_{diss}	0.989	0.984	0.967	0.990
η_{coll}	0.891	0.916	0.884	0.937

Table S15. EQE_{EL} of the queternary devices based on variant additives.

Device	EQE_{EL} ($\times10^{-4}$)
wo	3.032
DIO	2.940
DIB	2.966
DIO+DIB	3.078

Table S16. The detailed energy loss analysis of the quaternary PM6:D18-Cl:L8-BO:BTP-eC9 system.

Active layer	E_g (eV)	$V_{oc,sq}$ (V)	ΔE_1 (eV)	$J_{0,rad}$ (mA/cm^2)	$V_{oc,rad}$ (V)	ΔE_2 (eV)	V_{oc} (V)	ΔE_3 (eV)	E_{loss} (eV)
wo	1.448	1.183	0.265	8.686×10^{-18}	1.097	0.086	0.882	0.215	0.566
DIO	1.441	1.176	0.265	1.306×10^{-17}	1.087	0.090	0.869	0.218	0.572
DIB	1.432	1.168	0.264	1.000×10^{-17}	1.093	0.075	0.876	0.217	0.556
DIO+DIB	1.433	1.169	0.264	1.643×10^{-17}	1.081	0.088	0.868	0.213	0.565

Note:

The analysis of ΔE_3 is based on the equations below:

$$V_{oc,rad} \approx \frac{KTa}{q} ln\left(\frac{J_{ph}}{J_{o,rad}}\right)$$

$$\Delta E3 = \Delta V_{nr} = V_{oc,rad} - V_{oc}$$

Table S17. The detailed energy loss analysis of the quaternary PM6:D18-Cl:L8-BO:BTP-eC9 system.

Active layer	E_g (eV)	$V_{oc,sq}$ (V)	ΔE_1 (eV)	$J_{0,rad}$ (mA/cm^2)	$V_{oc,rad}$ (V)	ΔE_2 (eV)	V_{oc} (V)	ΔE_3 (eV)	E_{loss} (eV)
wo	1.448	1.183	0.265	0.209	0.882	1.091	0.092	0.566	1.448
DIO	1.441	1.176	0.265	0.210	0.869	1.079	0.098	0.572	1.441
DIB	1.432	1.168	0.264	0.210	0.876	1.086	0.082	0.556	1.432
DIO+DIB	1.433	1.169	0.264	0.209	0.868	1.077	0.092	0.565	1.433

Note:

The analysis of ΔE_3 is based on the equations below:

$$\Delta E3 = \Delta V'_{nr} \frac{KTa}{q} ln\left(\frac{1}{EQE_{EL}}\right)$$

References:

1. Yao, H. *et al.* 14.7% Efficiency Organic Photovoltaic Cells Enabled by Active Materials with a Large Electrostatic Potential Difference. *J. Am. Chem. Soc.* **141**, 7743–7750 (2019).
2. Yuan, J. *et al.* Single-Junction Organic Solar Cell with over 15% Efficiency Using Fused-Ring Acceptor with Electron-Deficient Core. *Joule* **3**, 1140–1151 (2019).
3. Yan, T. *et al.* 16.67% Rigid and 14.06% Flexible Organic Solar Cells Enabled by Ternary Heterojunction Strategy. *Adv. Mater.* **31**, 1902210 (2019).
4. Liu, S. *et al.* High-efficiency organic solar cells with low non-radiative recombination loss and low energetic disorder. *Nat. Photonics* **14**, 300–305 (2020).
5. Yu, R. *et al.* Improved Charge Transport and Reduced Nonradiative Energy Loss Enable Over 16% Efficiency in Ternary Polymer Solar Cells. *Adv. Mater.* **31**, 1902302 (2019).
6. Jiang, K. *et al.* Alkyl Chain Tuning of Small Molecule Acceptors for Efficient Organic Solar Cells. *Joule* **3**, 3020–3033 (2019).
7. An, Q. *et al.* Alloy-like ternary polymer solar cells with over 17.2% efficiency. *Science Bulletin* **65**, 538–545 (2020).
8. Zeng, Y. *et al.* Exploring the Charge Dynamics and Energy Loss in Ternary Organic Solar Cells with a Fill Factor Exceeding 80%. *Adv. Energy Mater.* **11**, 2101338 (2021).
9. Liu, Q. *et al.* Synergistically minimized nonradiative energy loss and optimized morphology achieved via the incorporation of small molecule donor in 17.7% efficiency ternary polymer solar cells. *Nano Energy* **85**, 105963 (2021).
10. Cui, Y. *et al.* Single-Junction Organic Photovoltaic Cells with Approaching 18% Efficiency. *Mater.* **32**, 1908205 (2020).
11. Li, S. *et al.* Unveiling structure-performance relationships from multi-scales in non-fullerene organic photovoltaics. *Nat. Commun.* **12**, 4627 (2021).
12. High-efficiency organic solar cells enabled by an alcohol-washable solid additive. *Sci. China Chem.* **64**, 2161-2168 (2021).
13. Li, C. *et al.* Non-fullerene acceptors with branched side chains and improved molecular packing to exceed 18% efficiency in organic solar cells. *Nat. Energy* **6**, 605–613 (2021).
14. Jiang, K. *et al.* Suppressed recombination loss in organic photovoltaics adopting a planar–mixed heterojunction architecture. *Nat. Energy* **7**, 1076–1086 (2022).
15. He, C. *et al.* Asymmetric electron acceptor enables highly luminescent organic solar cells with certified efficiency over 18%. *Nat. Commun.* **13**, 2598 (2022).
16. Song, J. *et al.* High-efficiency organic solar cells with low voltage loss induced by solvent additive strategy. *Matter* **4**, 2542–2552 (2021).
17. Bi, P. *et al.* Reduced non-radiative charge recombination enables organic photovoltaic cell approaching 19% efficiency. *Joule* **5**, 2408–2419 (2021).
18. Li, Y. *et al.* Mechanism study on organic ternary photovoltaics with 18.3% certified efficiency: from molecule to device. *Energy Environ. Sci.* **15**, 855-865 (2022).
19. He, C. *et al.* Versatile Sequential Casting Processing for Highly Efficient and Stable Binary Organic Photovoltaics. *Adv. Mater.* **34**, 2203379 (2022).
20. Sun, R. *et al.* Single-Junction Organic Solar Cells with 19.17% Efficiency Enabled by Introducing One Asymmetric Guest Acceptor. *Adv. Mater.* **34**, 2110147 (2022).

21. Cui, Y. *et al.* Single-Junction Organic Photovoltaic Cell with 19% Efficiency. *Adv. Mater.* **33**, 2102420 (2021).
22. Zhan, L. *et al.* Desired open-circuit voltage increase enables efficiencies approaching 19% in symmetric-asymmetric molecule ternary organic photovoltaics. *Joule* **6**, 662–675 (2022).
23. Li, C. *et al.* Achieving Record-Efficiency Organic Solar Cells upon Tuning the Conformation of Solid Additives. *J. Am. Chem. Soc.* **144**, 14731–14739 (2022).
24. He, C. *et al.* Manipulating the D:A interfacial energetics and intermolecular packing for 19.2% efficiency organic photovoltaics. *Energy Environ. Sci.* **15**, 2537–2544 (2022).
25. Wei, Y. *et al.* Binary Organic Solar Cells Breaking 19% via Manipulating the Vertical Component Distribution. *Advanced Materials* **34**, 2204718 (2022).
26. Wang, J. *et al.* Tandem organic solar cells with 20.6% efficiency enabled by reduced voltage losses. *National Science Review* **10**, nwad085 (2023).
27. Wang, J. *et al.* Binary Organic Solar Cells with 19.2% Efficiency Enabled by Solid Additive. *Adv. Mater.* **35**, 2301583 (2023).
28. Guan, S. *et al.* Balancing the Selective Absorption and Photon-to-Electron Conversion for Semitransparent Organic Photovoltaics with 5.0% Light-Utilization Efficiency. *Adv. Mater.* **34**, 2205844 (2022).
29. Bi, P. *et al.* Enhancing Photon Utilization Efficiency for High-Performance Organic Photovoltaic Cells via Regulating Phase-Transition Kinetics.*Adv. Mater.* **35**, 2210865 (2023).
30. Xu, X. *et al.* Sequential Deposition of Multicomponent Bulk Heterojunctions Increases Efficiency of Organic Solar Cells. *Adv. Mater.s* **35**, 2208997 (2023).
31. Zhu, L. *et al.* Single-junction organic solar cells with over 19% efficiency enabled by a refined double-fibril network morphology. *Nat. Mater.* **21**, 656–663 (2022).
32. Chen, T. *et al.* Compromising Charge Generation and Recombination of Organic Photovoltaics with Mixed Diluent Strategy for Certified 19.4% Efficiency. *Adv. Mater.* **35**, 2300400 (2023).
33. Song, W. *et al.* An in situ crosslinked matrix enables efficient and mechanically robust organic solar cells with frozen nano-morphology and superior deformability. *Energy Environ. Sci.* (2024) doi:10.1039/D4EE02724H.
34. Yu, Y. *et al.* Naphthalene diimide-based cathode interlayer material enables 20.2% efficiency in organic photovoltaic cells. *Sci. China Chem.* (2024) doi:10.1007/s11426-024-2244-8.
35. Guan, S. *et al.* Self-Assembled Interlayer Enables High-Performance Organic Photovoltaics with Power Conversion Efficiency Exceeding 20%. *Advanced Materials* **36**, 2400342 (2024).
36. Jiang, Y. *et al.* Non-fullerene acceptor with asymmetric structure and phenyl-substituted alkyl side chain for 20.2% efficiency organic solar cells. *Nat Energy* 1–12 (2024) doi:10.1038/s41560-024-01557-z.
37. Chen, C. *et al.* Molecular interaction induced dual fibrils towards organic solar cells with certified efficiency over 20%. *Nat Commun* **15**, 6865 (2024).
38. Zhu, L. *et al.* Achieving 20.8% organic solar cells via additive-assisted layer-by-layer fabrication with bulk *p-i-n* structure and improved optical management. *Joule* (2024) doi:10.1016/j.joule.2024.08.001.